

## Representation of the Heated Planetary Boundary Layer in Mesoscale Models with Coarse Vertical Resolution

ROGER A. PIELKE<sup>1</sup> AND YITZHAQ MAHRER

*Department of Environmental Sciences, University of Virginia, Charlottesville 22903*

(Manuscript received 22 April 1975, in revised form 25 August 1975)

### ABSTRACT

This paper uses a prognostic equation suggested by Deardorff for the growth of the planetary boundary layer to close the parameterization scheme for vertical turbulent mixing in the planetary boundary layer. The following major conclusions are obtained:

- 1) The prognostic equation for the growth of the planetary boundary layer is much superior to the diagnostic form used earlier by Pielke.
- 2) The growth of the planetary boundary layer into a region with substantial vertical shear of the horizontal wind markedly alters the locations of sea-breeze convergence zones.
- 3) By improving the boundary layer parameterization scheme given in Pielke, the simulation of vertical turbulent mixing by eddy coefficients which are a function of distance from the ground results in predictions which are as good as those obtained with Deardorff's much more sophisticated model, and agree favorably with those observed during Day 33 of the Wangara experiment.
- 4) The effect of decreasing the resolution from 31 levels to 8 levels in the boundary layer parameterization scheme does not seriously degrade the solutions, implying that the scheme discussed in this paper is a useful tool to represent the heated boundary layer in mesoscale models.

### 1. Introduction

The surface fluxes of momentum, heat and moisture and their distribution with height are important in determining the form of atmospheric circulations ranging from the global scale down to the individual cloud scale and even smaller. An accurate parameterization of the heated planetary boundary layer is, therefore, essential if the atmosphere is to be simulated properly in a numerical model.

There are currently at least three main ways to treat planetary-boundary-layer mixing in those models which have a number of grid points in that layer. These methods range from an eddy exchange coefficient profile, which is a function of distance from the top of the surface layer, to locally-derived exchange coefficients, and finally, to explicit time-dependent equations for the turbulent fluctuations. Lee (1973) and Pielke (1974a) have developed models which use the profile function approach, while Deardorff (1973) and Orlanski *et al.* (1974) have developed eddy coefficients which are dependent on only local gradients of dependent variables. Lumley and Khajeh-Nouri (1974), Donaldson (1973) and Deardorff (1974) have developed explicit dynamic equations for the subgrid-scale fluxes, which are solved by making closure assumptions for the higher-order

moments of turbulence. Mellor and Yamada (1974) have investigated the ability of the explicit equations to simulate turbulence in the planetary boundary layer using four levels of closure which are of varying complexity and completeness.

The use of dynamic equations to describe subgrid-scale processes would appear to be the most desirable approach on physical grounds, since the mathematical system, which is designed to represent the real world, has more degrees of freedom and, therefore, would be expected to better represent nature. Unfortunately, the addition of time-dependent equations to calculate the subgrid-scale fluxes in a numerical model, even for dry isentropic motion, requires the solution of 18 additional equations as well as the storage of at least 36 additional variables (since more than one time level is required) at each grid point on the computer.<sup>2</sup> The added number of calculations and dependent variables limit the simulation of the planetary boundary layer by this technique to only specialized situations such as dry isentropic motion over horizontally homogeneous terrain under steady large-scale conditions. Moreover, the investigator must have access to the latest generation computer and must have been allocated sufficient computer resources to do the job.

The use of locally-dependent exchange coefficients to represent subgrid-scale fluxes relaxes the computer

<sup>1</sup> Also affiliated with the Center for Advanced Studies, University of Virginia.

<sup>2</sup> W. R. Cotton, personal communication.

requirement somewhat, although in order for the exchange coefficient to be "reasonably local," the vertical grid separation must necessarily be small. In this approach, the exchange coefficients are assumed proportional to local gradients of shear, to local gradients of buoyancy, and/or to the local turbulent energy. Orlanski *et al.* (1974), for example, use a coefficient in their 80-level, two-dimensional mesoscale model which is proportional only to the local vertical gradients of potential temperature. Deardorff (1975) has introduced a coefficient which is proportional to the local turbulent energy.

Even with a two-dimensional simulation, however, the large number of grid points required to satisfactorily use a locally-dependent exchange coefficient requires considerable computer-resource allocation as well as a sophisticated advanced-generation machine capable of handling the large number of data points. When we extend the model to the third spatial dimension, as in Deardorff's (1973) planetary boundary layer model, the computer resources required become unobtainable for most researchers, and even when such resources are available, the number of simulation cases which can be run are severely limited.

Therefore, although the use of dynamic equations for the subgrid-scale fluxes or the assumption of locally-dependent exchange coefficients are more desirable representations of subgrid turbulence, the cruder parameterization of the planetary boundary layer using the profile function technique will be used in most numerical models which resolve the planetary boundary layer for the foreseeable future.

This paper will examine the adequacy of the profile-function approach using two-dimensional and one-dimensional versions of the mesoscale model developed by Pielke (1974a). As shown by Pielke (1974b), a two-dimensional representation is an economical way to examine the theoretical aspects of mesoscale circulations, although simulations of actual atmospheric systems will, in general, not be realistic without including the third spatial dimension. The one-dimensional model is an efficient way to investigate the adequacy of the planetary boundary layer scheme without considering effects other than vertical turbulent mixing in a geostrophic flow field.

Using the model, answers to the following questions will be sought:

1) Does the representation of the growth of the planetary boundary layer suggested by Deardorff (1974) produce a more realistic solution than that used by Pielke (1974a) in his simulation of the sea breezes over south Florida?

2) How important is the change in depth of the planetary boundary layer on the development and movement of sea-breeze convergence zones over a heated island?

3) How well can the profile-function technique predict observed planetary boundary layer structure during the day?

## 2. Model

Because details of the model have been reported by Pielke (1974a, b), only recent changes to the model will be mentioned here. The equations used by Pielke in those papers consisted of prognostic and diagnostic equations for the grid-volume-averaged perturbations from a larger scale state. Since that work, it was found that the total resolvable dependent variables, grid-volume-averaged perturbations plus large-scale values, could be integrated as one variable. Almost identical solutions were obtained with an increase of around 10% in calculation efficiency. Permitting time variations in the large-scale variables introduced the effect of inertial motions on that scale, but those motions were masked by the more dominant mesoscale-initiated flow.

The form of the equations currently used in the two-dimensional version of the model, are given below (symbols defined in the Appendix):

*East-west equation of motion*

$$\frac{\partial u}{\partial t} = -u \frac{\partial u}{\partial x} - w \frac{\partial u}{\partial z} - \theta \frac{\partial \pi}{\partial x} + f_3 v - f_2 w + \frac{\partial}{\partial z} \left[ K_z^{(m)} \frac{\partial u}{\partial z} \right] + \frac{\partial}{\partial x} \left[ K_H \frac{\partial u}{\partial x} \right] \quad (1)$$

*North-south equation of motion*

$$\frac{\partial v}{\partial t} = -u \frac{\partial v}{\partial x} - w \frac{\partial v}{\partial z} + f_3 u_a - f_3 u + \frac{\partial}{\partial z} \left[ K_z^{(m)} \frac{\partial v}{\partial z} \right] + \frac{\partial}{\partial x} \left[ K_H \frac{\partial v}{\partial x} \right] \quad (2)$$

*Potential temperature equation*

$$\frac{\partial \theta}{\partial t} = -u \frac{\partial \theta}{\partial x} - w \frac{\partial \theta}{\partial z} + \frac{\partial}{\partial z} \left[ K_z^{(\theta)} \frac{\partial \theta}{\partial z} \right]^* + \frac{\partial}{\partial x} \left[ K_H \frac{\partial \theta}{\partial x} \right] \quad (3)$$

*Specific humidity equation*

$$\frac{\partial q}{\partial t} = -u \frac{\partial q}{\partial x} - w \frac{\partial q}{\partial z} + \frac{\partial}{\partial z} \left[ K_z^{(q)} \frac{\partial q}{\partial z} \right] + \frac{\partial}{\partial x} \left[ K_H \frac{\partial q}{\partial x} \right] \quad (4)$$

\* Deardorff (1967) suggests this term should be modified to permit countergradient heat fluxes as observed in most observational experiments. His proposed form in clear air for the heat flux is

$$\overline{w'\theta'} = -K_z^{(\theta)} \left( \frac{\partial \theta}{\partial z} - 0.7^\circ \text{K km}^{-1} \right).$$

Clarke *et al.* (1971), however, observed no countergradient heat flux on Day 33 of their Wangara experiments, and since their data are used in Section 4 of this paper to verify the model, the flux term as given in (3) will be used.

*Incompressible continuity equation*

$$\frac{\partial w}{\partial z} = -\frac{\partial u}{\partial x} \tag{5}$$

*Hydrostatic equation*

$$\frac{\partial \pi}{\partial z} = -\frac{g}{\theta} \tag{6}$$

In the above dependent variables represent averages over a grid volume. The variable  $\pi$ , henceforth called pressure, is defined as

$$\pi = C_p \left( \frac{P}{P_{00}} \right)^\kappa$$

The diagnostic equations (5) and (6) are solved by the upward integration of (5) from a rigid bottom ( $w=0$ ), corresponding to the ground, while (6) is integrated downward from an upper material surface. The height of the upper surface is capable of responding to heating in lower layers, as explained by Pielke (1974a), and its depth is calculated from

$$\frac{\partial s}{\partial t} = -u \frac{\partial s}{\partial x} + w_T - \int_{z_T}^{s(t)} \frac{\partial u}{\partial x} dz \tag{7}$$

This form of the equation for the growth of the upper surface was adapted from Lavoie (1972). The pressure  $\pi$  on  $s$  at time  $t$ , required in the downward integration of (6), is calculated from

$$\pi[s(t)] = \hat{\pi} - \frac{g}{\theta} [s(t) - \hat{s}], \tag{8}$$

where the caret indicates an initial value, and  $\hat{\theta}$  is the vertical mean potential temperature in the layer between  $s$  and  $\hat{s}$ . In the original model discussed in Pielke (1974a, b), the hydrostatic equation was integrated upward from the surface, where the surface value was determined from a tendency equation which was proportional to the integrated, potential temperature changes above that level. Using both techniques to calculate  $\pi$  as a function of height resulted in almost identical solutions, so the new method was adopted in the model, since one calculation step was eliminated.

The form of the horizontal exchange coefficients  $K_H$  is given by

$$K_H = \alpha_{2D} (\Delta x)^2 \left[ \left( \frac{\partial v}{\partial x} \right)^2 + \frac{1}{2} \left( \frac{\partial u}{\partial x} \right)^2 \right]^{\frac{1}{2}}$$

where the appropriate value of  $\alpha_{2D}$  was obtained by Pielke (1974b), as that value which gave the best agreement with the three-dimensional model under equivalent initial and boundary conditions when the forcing was two-dimensional.

Of central interest in the paper is the form of the vertical-exchange coefficients,  $K_z^{(m)}$ ,  $K_z^{(\theta)}$ ,  $K_z^{(q)}$ . The functional form of this term, used by Pielke (1974a, b), is

$$K_z^{(n)} = \begin{cases} K_z^{(n)}|_{z_i} + [(z_i - z)^2 / (z_i - h)^2] \\ \quad \times [K_z^{(n)}|_h - K_z^{(n)}|_{z_i} + (z - h) \\ \quad \times \{(\partial/\partial z)K_z^{(n)}|_h \\ \quad + 2((K_z^{(n)}|_h - K_z^{(n)}|_{z_i}) / (z_i - h))\}], & z_i \geq z \geq h \\ K_z^{(n)}|_{z_i}, & z > z_i \\ (z/h)K_z^{(n)}|_h, & z < h \end{cases} \tag{9}$$

where  $K_z^{(n)}$  refers to either one of the three vertical exchange coefficients. In the model  $K_z^{(\theta)}$  is assumed identical to  $K_z^{(q)}$ . The form of  $K_z^{(n)}$  above  $h$  was suggested by O'Brien (1970), while the value of  $K_z^{(n)}|_h$  was evaluated based on surface-layer theory introduced by Yamamoto and Shimanuki (1966) with corresponding interpolation formulas for the profile functions developed by Shimanuki (1969). The value of  $K_z^{(n)}|_{z_i}$  was assumed as  $1 \text{ cm}^2 \text{ s}^{-1}$ . With stable air in the surface layer, the coefficients for momentum, heat and moisture are assumed identical, while with unstable air near the surface, the coefficients for heat and moisture are larger. A schematic picture of the functional form of  $K_z^{(n)}$  is given in Fig. 1.

In Sections 2 and 3, the vertical-turbulent fluxes are evaluated by calculating exchange coefficients using (9) and multiplying them by the vertical gradient of the appropriate dependent variable. In Section 4, where the model is reduced to one dimension and compared against observations, the parameterization of the vertical-turbulent-flux terms is improved. These changes will be discussed in that section.

As pointed out by O'Brien (1970), Eq. (9) cannot be evaluated until the values of  $z_i$  and  $h$  are determined or assigned. In past models, such as those of Estoque (1961, 1962) and McPherson (1970), these levels have been assigned arbitrarily and kept constant throughout an integration.

As is well known, however, on most days the planetary boundary layer grows in response to surface heat fluxes, so a constant value of  $z_i$  is incorrect.

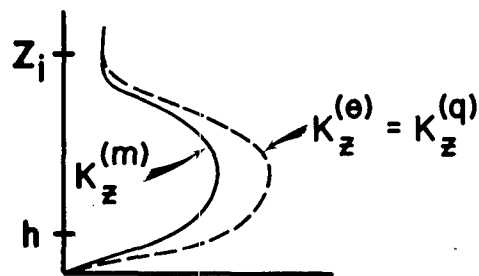


FIG. 1. A schematic illustration of the vertical profile of the vertical eddy exchange coefficient  $K_z^{(n)}$ .

To permit variations in  $z_i$ , Pielke (1974a, b) recently used a formulation proposed by Blackadar (personal communication) given by

$$z_i = 0.25u_* / f_3. \tag{10}$$

As mentioned by Blackadar, this form is only valid for steady-state, horizontally homogeneous flow in a neutrally stratified atmosphere. In unstable air, he suggests  $z_i$  is also a function of the stability, and that  $z_i$  is larger in unstable air. Deardorff (1973), however, proposed that  $z_i$  was determined by an inversion level rather than by some fraction of  $u_* / f_3$ . During the development of the model presented in Pielke (1974a,b), there was sufficient disagreement among acknowledged experts as to the appropriate functional specification of  $z_i$  that it was decided to use (10) under all lapse-rate conditions in the model. Undoubtedly an improvement over a constant  $z_i$ , Eq. (10) was used under conditions for which there was no theoretical justification, and an improvement to (10) must be found.

Recently, Deardorff (1974) has proposed a prognostic equation for  $z_i$ , based on numerical results with his sophisticated planetary-boundary-layer model and on laboratory studies, which in comparison with boundary-layer observations accurately represents the growth of the planetary boundary layer during clear days. In terms of the model variables discussed in this paper, his equation for  $z_i$  can be written as

$$\frac{\partial z_i}{\partial t} = -u \frac{\partial z_i}{\partial x} + w_i + \frac{1.8(w_*^3 + 1.1u_*^3 - 3.3u_*^2 f_3 z_i)}{z_i^2 \frac{\partial \theta^+}{\partial z} + 9w_*^2 + 7.2u_*^2}, \tag{11}$$

where at the initial time  $z_i$  is assumed equal to a synoptic or large-scale value, such as might be obtained from an early-morning inversion as observed by a radiosonde.

Deardorff (personal communication) emphasizes that this formulation is invalid on days with cumulus clouds rooted in the planetary boundary layer unless the vertical velocity term  $w_i$  includes cumulus-induced subsidence, as well as larger scale ascent and descent. With the exception of a continuous deck of strato-cumulus cloud, Deardorff suggests for this situation that  $z_i$  and the lifting condensation level will rise together, once  $z_i$  initially reaches the condensation level, provided cumulus-induced subsidence is treated properly. In the current paper, no such cumulus effect is considered.

The value of  $w_*$  is given as

$$w_* = \begin{cases} \left( \frac{-g}{\theta_*} u_* \theta_* z_i \right)^{\frac{1}{2}}, & \theta_* \leq 0 \\ 0, & \theta_* > 0 \end{cases}$$

where  $u_*$  and  $\theta_*$  are evaluated for the experiments in this section and Section 3 by Eqs. (20) and (21) in

Pielke (1974a). In Section 4,  $u_*$  and  $\theta_*$  are evaluated by the improved method given by (24) and (25).

In the limiting case with overlying, neutrally stratified air, no surface heat flux, horizontal advection or vertical motion, the steady-state solution of (11) reduces to

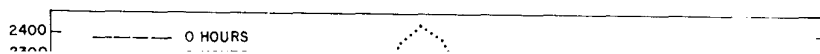
$$z_i = 0.33u_* / f_3, \tag{12}$$

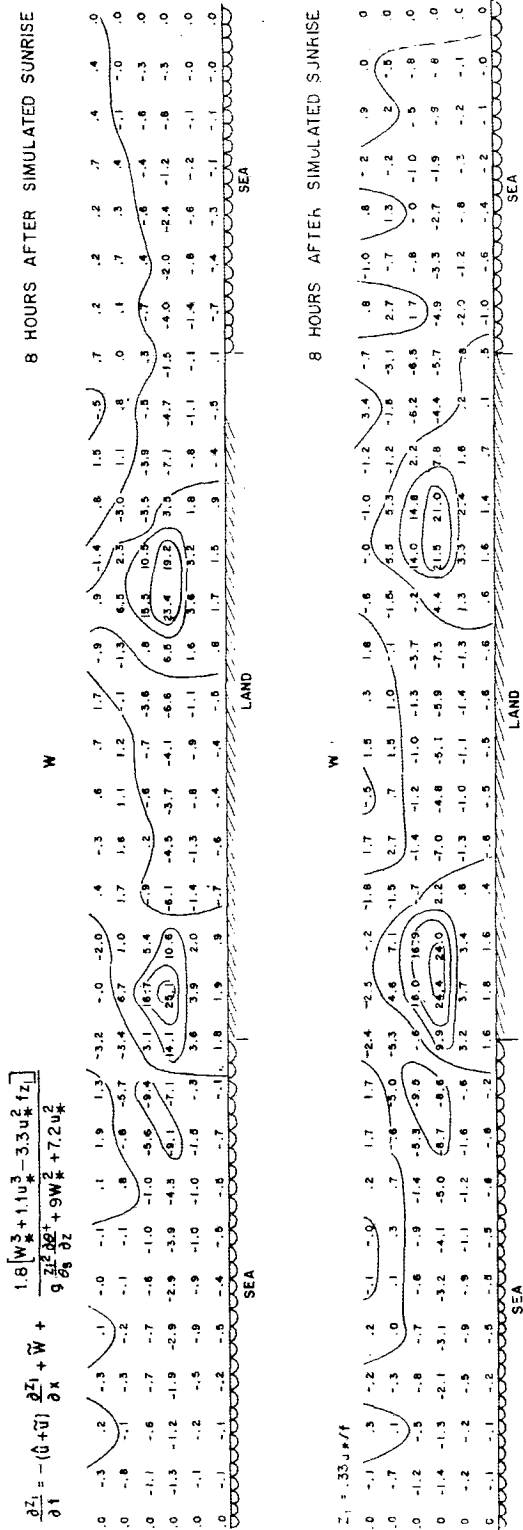
which is the equivalent of (10).

To test the two formulations given by (11) and (12), two experiments were performed where everything was identical, except for the specification of  $z_i$ . The initial and lateral boundary conditions are the same as used in the experiment given in Section 5 of Pielke (1974b) where  $\alpha_{2D} = 1.428$ . In that experiment, a heated land strip was prescribed from grid point  $11\frac{1}{2}$  to grid point  $25\frac{1}{2}$ , or a simulated distance of 154 km. The surface roughness  $z_0$  over land was assumed as 4 cm, while the temperature at that level over land was a sinusoidal function of time with a maximum amplitude of 10 K above that of the water and with a half-period of 13 h, 44 min. Over water, the temperature at  $z_0$  is assumed constant, while  $z_0$  is calculated as a function of  $u_*$  and  $g$  as discussed by Pielke (1974a). The geostrophic wind is from the east at  $2.5 \text{ m s}^{-1}$ . The depth  $h$  of the surface layer is computed in the same manner in both experiments as  $h = 0.04z_i$ . This expression for  $h$  was based on the results of Blackadar and Tennekes (1968) for a neutrally stratified boundary layer where a value of  $h$  equal to 4% of  $z_i$  gave the best agreement with observations. The level at which surface layer theory fails significantly needs more investigation.

The vertical motions for the two experiments, 8 h after sunrise, are given in Figs. 2 and 3. Along the lee coast, the two solutions are similar, although the vertical motion maximum is somewhat broader when the diagnostic form of determining  $z_i$  is used. The magnitudes are similar, however. The windward convergence zone should be more sensitive to the different techniques to evaluate  $z_i$ , since it is a moving system, in contrast to the leeward convergence zone which remains more or less stationary. As seen in the two figures, the convergence zone is one grid point or 11 km further inland when  $z_i$  is determined using the prognostic equation, although again the magnitudes of vertical motion are very similar.

It is somewhat surprising that the solutions should be so much alike, particularly when we look at Figs. 4 and 5 where the spatial distributions of  $z_i$ , as a function of time for the two methods, are displayed. When the diagnostic method of computing  $z_i$  is used (Fig. 4), the values are extremely irregular and confusing, with a local minimum of  $z_i$  in the middle of the convergence zone. The complicated pattern of  $z_i$  is a result of the direct dependence of  $z_i$  on  $u_*$  and, therefore, on the low-level winds. In the center of the convergence zone, for example, the value of  $z_i$  must necessarily be relatively





Figs. 2 and 3. The vertical motion field ( $\text{cm s}^{-1}$ ) 8 h after sunrise with Eq. (12) [Fig. 2 (bottom)] and Eq. (11) [Fig. 3 (top)].

small because the low-level winds have decelerated in order to generate the low-level convergence.

In contrast to the diagnostic method of evaluating  $z_i$ , however, the prognostic technique suggested by Deardorff (1974) produces very realistic solutions with the planetary boundary layer growing over the land as the surface is heated, with the highest levels in the convergence zone where  $w_i$  is the largest.

The degree of agreement between the two experiments must be partially fortuitous since, as surface heating develops during the day, the stress contribution in (11) rapidly becomes unimportant relative to the heat flux term. The values of  $z_i$  using the two methods are reasonably well correlated near the convergence zone only because the acceleration of the wind into the convergence zone results in higher  $u_*$  values; therefore  $z_i$  using the diagnostic technique is larger, in agreement with the prognostic method. Only if the  $z_i$  values were reasonably well correlated could the solutions, as illustrated in Figs. 2 and 3, be so similar. However, since there is no guarantee that this correlation would exist for all mesoscale problems, the diagnostic equation for  $z_i$  is a poor representation of the depth of the planetary boundary layer and should be discarded and replaced by the prognostic technique introduced by Deardorff.

### 3. Influence of vertical shear of the geostrophic wind

In order to study the importance of the growth of the planetary boundary layer on sea breeze circulations, a series of experiments were performed which were equivalent to those given in Fig. 5, except that a non-zero geostrophic wind shear was assumed above the level of the synoptic planetary boundary layer. Two cases of shear were assumed: one with increasing easterly geostrophic shear, the other with increasing westerly shear. The magnitude of the geostrophic shear are given by

$$\frac{\partial u_g}{\partial z} = \begin{cases} 3 \text{ m s}^{-1} \text{ km}^{-1}, & z > \hat{z}_i = 252 \text{ m} \\ 0, & z \leq \hat{z}_i \end{cases}$$

with  $u_g|_{\hat{z}_i} = -2.5 \text{ m s}^{-1}$  for Case I, and

$$\frac{\partial u_g}{\partial z} = \begin{cases} -3 \text{ m s}^{-1} \text{ km}^{-1}, & z > \hat{z}_i = 252 \text{ m} \\ 0, & z \leq \hat{z}_i \end{cases}$$

with  $u_g|_{\hat{z}_i} = -2.5 \text{ m s}^{-1}$  for Case II, where  $\hat{z}_i$  is the initial depth of the planetary boundary layer. In the Control Case the geostrophic shear is identically zero.

An additional term is implied when there is geostrophic shear, i.e., a vertical shear of the geostrophic wind implies a horizontal gradient of potential temperature. For the two-dimensional model this can be shown the following way. The east-west geostrophic wind is defined in terms of the synoptic variables and is given

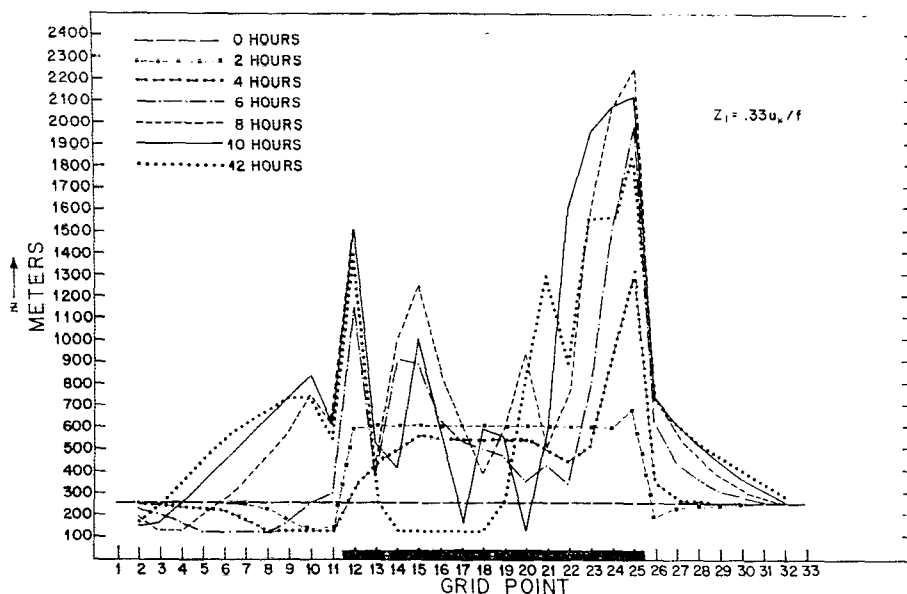


FIG. 4. The spatial distribution of  $z_i$  as a function of time when  $z_i$  is computed by the diagnostic method.

by

$$u_g = -\frac{\hat{\theta}}{f_s} \frac{\partial \hat{\pi}}{\partial y} \quad (13)$$

By differentiating (13) with respect to  $z$  and using the hydrostatic relation along with the definition of the geostrophic wind given by (13), the geostrophic shear can be written as

$$\frac{\partial u_g}{\partial z} = \frac{u_g}{\hat{\theta}} \frac{\partial \hat{\theta}}{\partial z} - \frac{g}{f_s \hat{\theta}} \frac{\partial \hat{\theta}}{\partial y} \quad (14)$$

The first term on the right-hand side of (14) implies a geostrophic wind shear whenever there is a vertical potential temperature gradient. This term arises because, as seen from (13), a change in  $\hat{\theta}$  obviously changes the geostrophic wind.

To make the inclusion of geostrophic shear in the east-west velocity consistent, it is therefore necessary to evaluate a synoptic-scale north-south potential

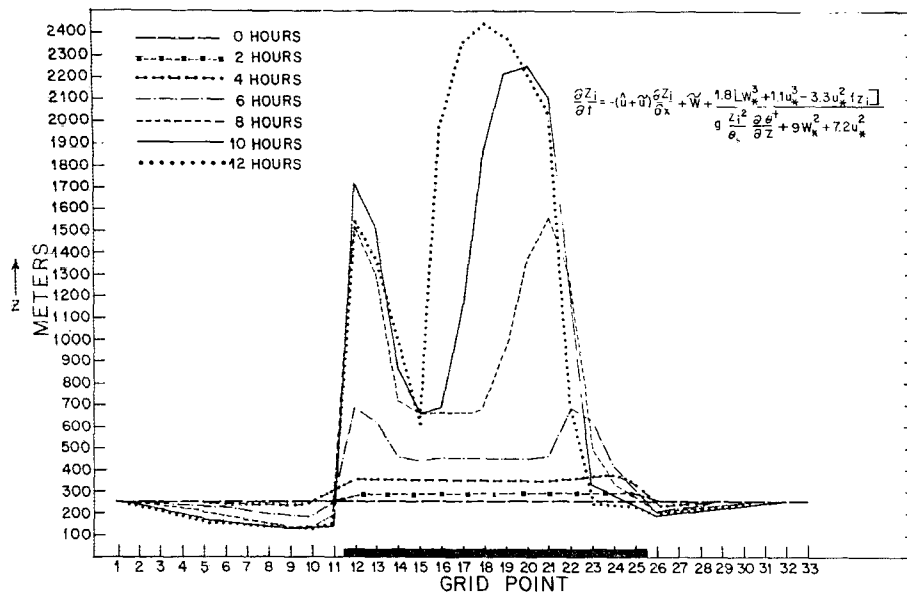


FIG. 5. The spatial distribution of  $z_i$  as a function of time when  $z_i$  is computed by the prognostic method.

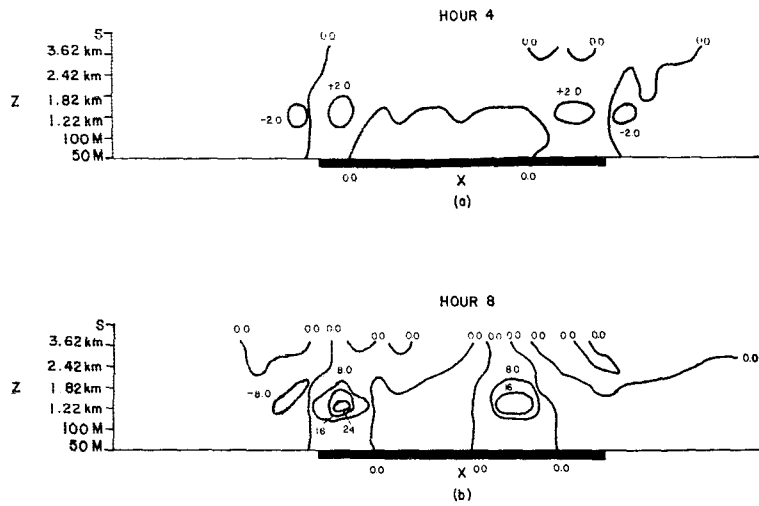


FIG. 6. The vertical motion field ( $\text{cm s}^{-1}$ ) 4 h (a) and 8 h (b) after simulated sunrise for

$$u_g|_{z_i} = -2.5 \text{ m s}^{-1}; \quad \left. \frac{\partial u_g}{\partial z} \right|_{\text{above } z_i} = 0.0 \text{ (Control Case).}$$

temperature gradient which is given by

$$\frac{\partial \hat{\theta}}{\partial y} = -\frac{f_3 \hat{\theta}}{g} \frac{\partial u_g}{\partial z} + \frac{f_3 u_g}{g} \frac{\partial \hat{\theta}}{\partial z} \quad (15)$$

The magnitude of this term, for example, with a geostrophic shear of  $3 \text{ m s}^{-1} \text{ km}^{-1}$  and with the synoptic thermodynamic soundings and Coriolis parameter used

previously, results in a north-south potential temperature gradient of at most  $0.59^\circ\text{C} (100 \text{ km})^{-1}$ . Calculations performed with and without term (15) had no significant effect on the solution. After 10 h of simulation, differences in the magnitude in the vertical motion field were less than  $0.1 \text{ cm s}^{-1}$ . This term would undoubtedly be more important with stronger geostrophic shears such as near frontal zones. For the experiments

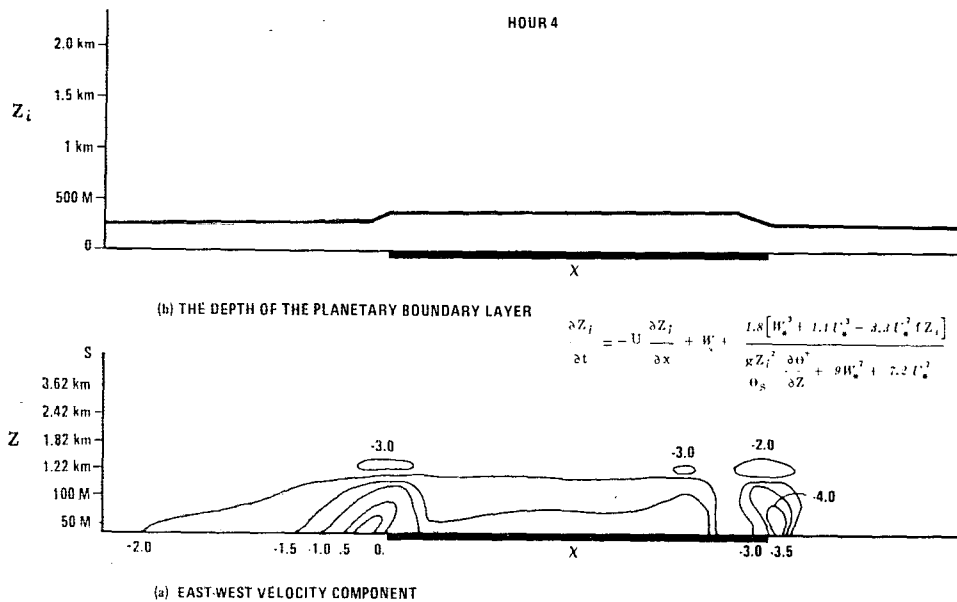


FIG. 7. The east-west velocity component (a) and the depth of the planetary boundary layer (b) 4 h after simulated sunrise for

$$u_g|_{z_i} = -2.5 \text{ m s}^{-1}; \quad \left. \frac{\partial u_g}{\partial z} \right|_{\text{above } z_i} = 0.0 \text{ (Control Case).}$$

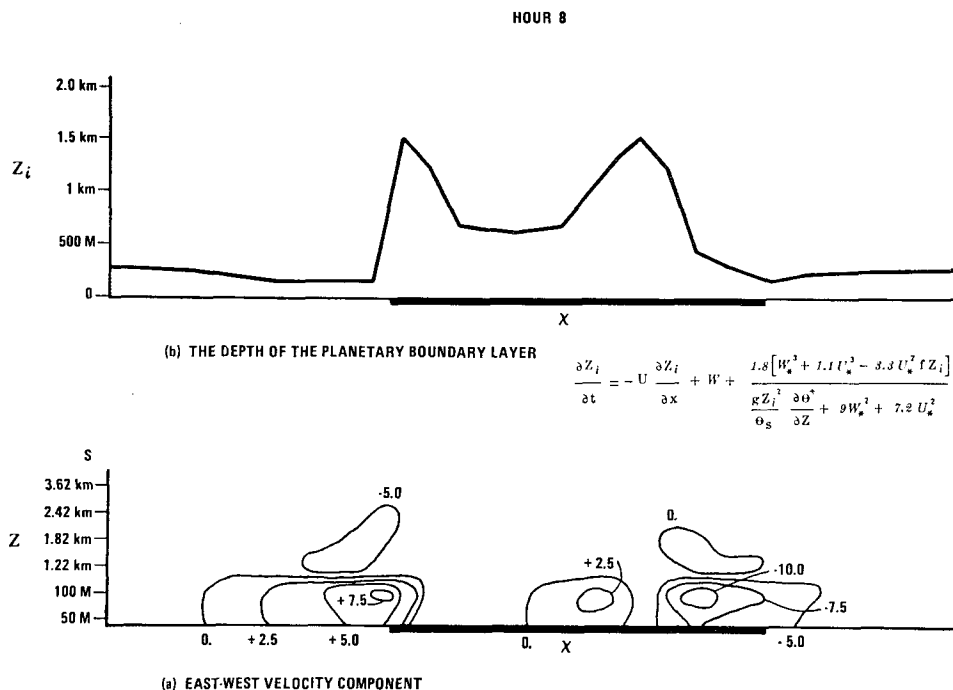


FIG. 8. As in Fig. 7 except for 8 h after simulated sunrise.

presented in this paper, however, the contributions of the horizontal synoptic temperature gradient to the dynamics of the sea-breeze circulations are negligible.

Returning to the suggested formulation for the growth of the planetary boundary layer given by (11), we see that this expression for  $z_i$  permits the incorporation of existing upper-level wind shear into the planetary boundary layer as it deepens during the day. This

was not possible in earlier specifications of the planetary boundary layer depth in mesoscale models, except for that used by Pielke (1974a) and, as shown earlier, that form is not realistic. Recent work by Emmitt (1975) has suggested the sign and magnitude of the upper level shear is crucial in determining the occurrence or non-occurrence of rainfall over Barbadoes on synoptically undisturbed days.

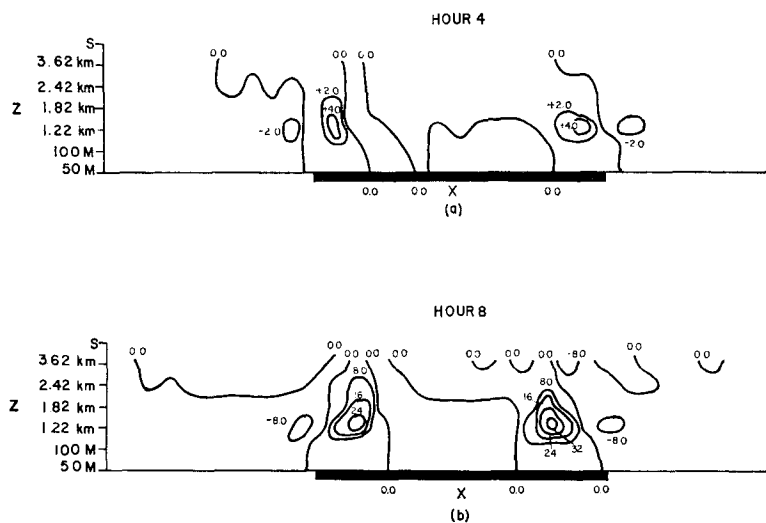


FIG. 9. The vertical motion field ( $\text{cm s}^{-1}$ ) 4 h (a) and 8 h (b) after simulated sunrise for

$$u_y|_{z_i} = -2.5 \text{ m s}^{-1}; \quad \left. \frac{\partial u_y}{\partial z} \right|_{\text{above } z_i} = 3 \text{ m s}^{-1} \text{ km}^{-1} \text{ (Case I).}$$

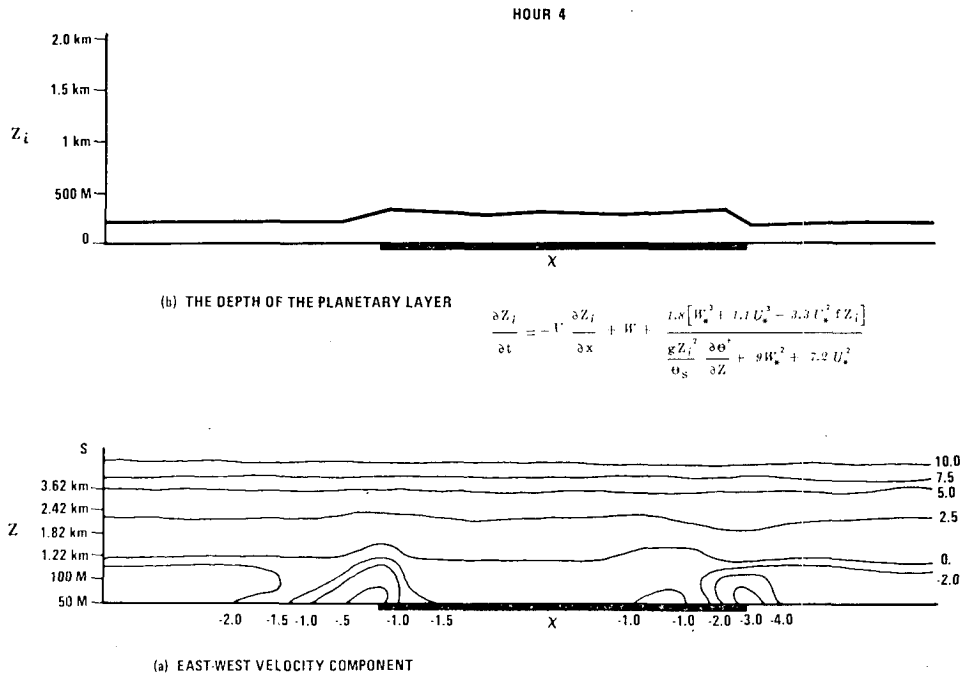


FIG. 10. The east-west velocity component (a) and the depth of the planetary boundary layer (b) 4 h after simulated sunrise for

$$u_y|_{z_i} = -2.5 \text{ m s}^{-1}; \quad \left. \frac{\partial \theta_0}{\partial z_i} \right|_{\text{above } z_i} = 3 \text{ m s}^{-1} \text{ km}^{-1} \text{ (Case I).}$$

The east-west velocity, depth of  $z_i$ , and the vertical motion field are shown in Figs. 6 through 14 for Case I, Case II and the Control Case at 4 and 8 h after sunrise. In the Control Case there is no overlying geostrophic wind shear, while in Case I the geostrophic wind be-

comes more westerly with height, and in Case II the geostrophic wind becomes more easterly with height. The magnitude of the shear in Case I and Case II are identical.

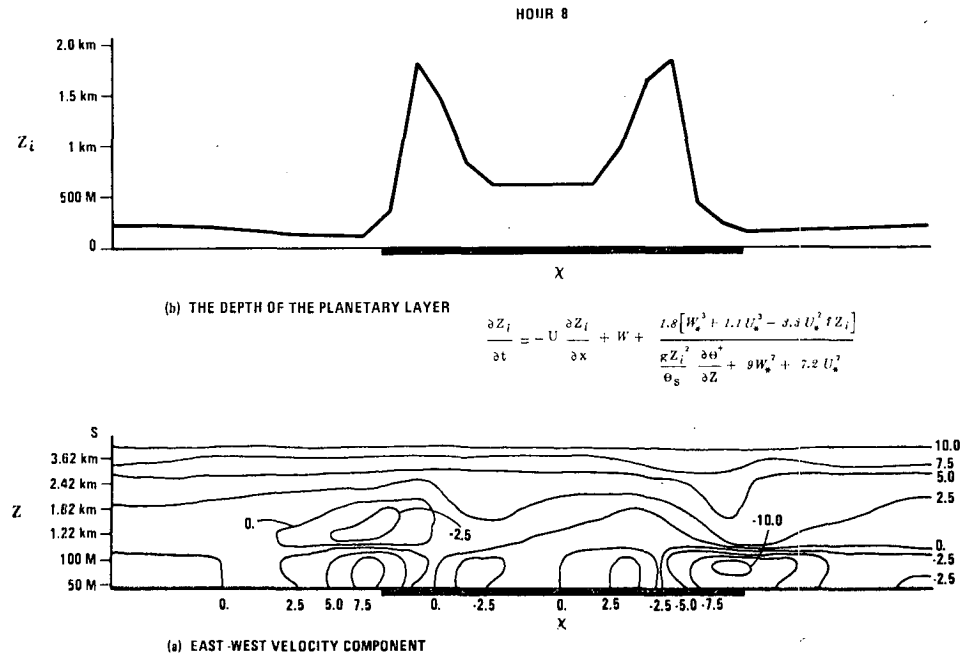


FIG. 11. As in Fig. 10 except for 8 h after simulated sunrise.

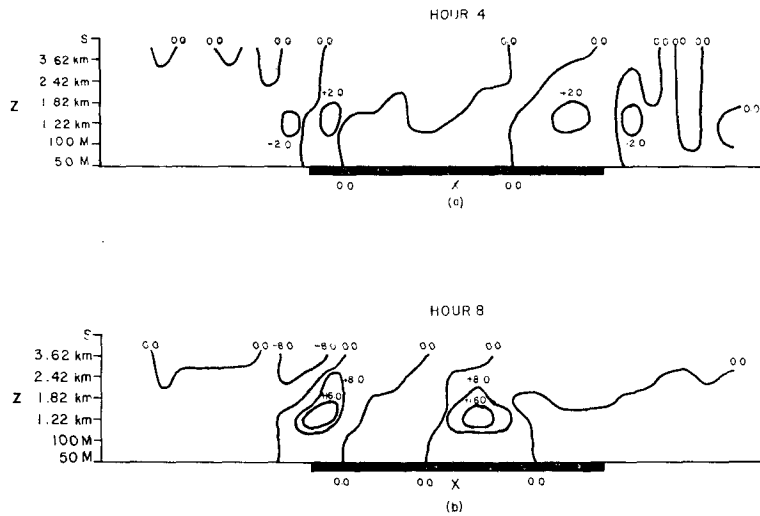


FIG. 12. The vertical motion field (cm s<sup>-1</sup>) 4 h (a) and 8 h (b) after simulated sunrise for

$$u_p|_{z_i} = -2.5 \text{ m s}^{-1}; \quad \left. \frac{\partial u_p}{\partial z_i} \right|_{\text{above } z_i} = -3 \text{ m s}^{-1} \text{ km}^{-1} \text{ (Case II)}.$$

The results after 4 h are very similar between the three experiments. Apparently, the boundary layer has not grown sufficiently to significantly tap the upper-level winds in Case I and Case II. After 8 h, however, the solutions diverge from one another. In Case II, where the winds become more easterly with height, the eastern convergence zone is much further inland than

in the Control Case, although the magnitudes of vertical motion are approximately the same. In addition, the western region of upward motion is significantly weaker and lies immediately along the western coastline. As evident in the plot of  $z_i$  in Fig. 14, the boundary layer has grown sufficiently to tap the stronger easterlies aloft, mix them downward, and thereby cause an

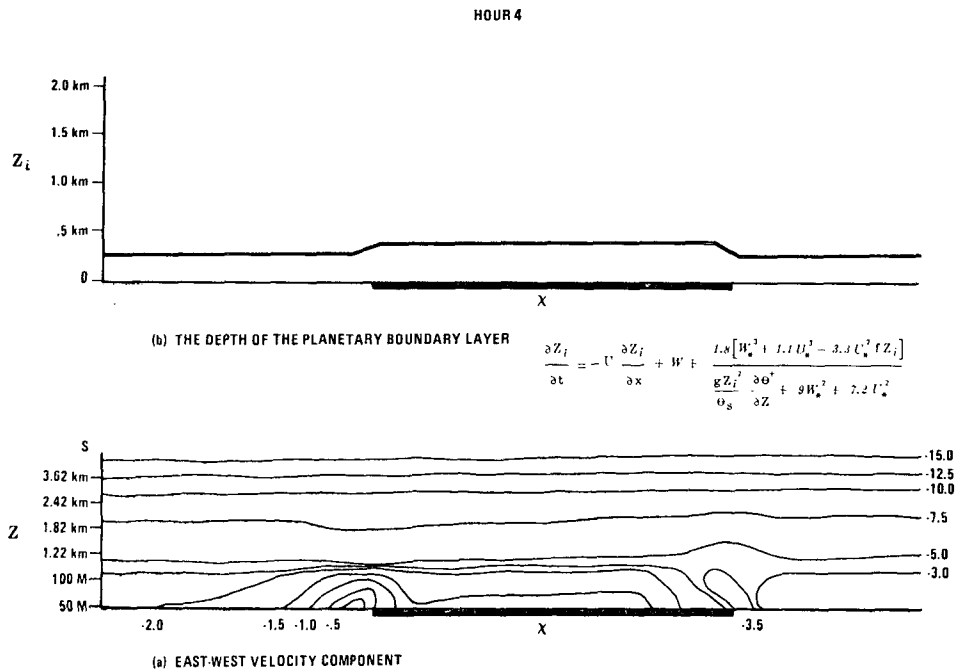


FIG. 13. The east-west velocity component (a) and the depth of the planetary boundary layer (b) 4 h after simulated sunrise for

$$u_p|_{z_i} = -2.5 \text{ m s}^{-1}; \quad \left. \frac{\partial u_p}{\partial z_i} \right|_{\text{above } z_i} = -3 \text{ m s}^{-1} \text{ km}^{-1} \text{ (Case II)}.$$

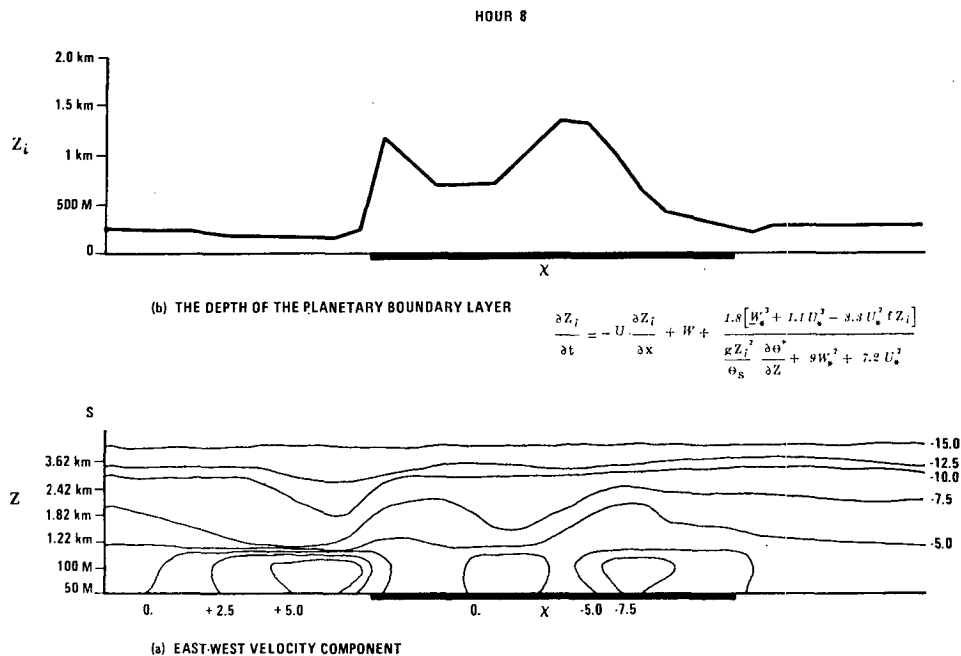


FIG. 14. As in Fig. 13 except for 8 h after simulated sunrise.

acceleration of both convergence zones toward the west. The downward transport of stronger easterlies has also weakened the intensity of the leeward convergence zone. After 12 h, in fact (not shown), the western convergence zone has shifted slightly offshore in response to the decrease of onshore accelerations as land heating dies off, but with the continued downward transport of offshore momentum through the deep boundary layer.

In Case I after 8 h, in contrast, where the geostrophic winds become more westerly with height, the eastern convergence zone is retarded in its westward movement relative to the Control Case and has substantially stronger vertical velocities, while the western convergence zone is accelerated inland with about the same upward motions as in the Control. With the geostrophic wind becoming more westerly with height, the downward transfer of momentum accelerates the flow toward the east.

These results demonstrate that, although the low-level wind controls the general movement inland of one convergence zone and the retardation of the movement inland of the other, the details of the propagation of the convergence zones are substantially altered by the downward transport of horizontal momentum, whenever the planetary boundary layer deepens sufficiently to include the higher winds aloft. When the vertical shear of the large-scale wind is the same sign as the low-level winds, the convergence zone is closer to the lee coast and is decreased in magnitude relative to when no shear is present; the windward convergence zone, on the other hand, is further inland and relatively unchanged in intensity. In contrast, when the vertical shear is of the opposite sign to the low-level winds, the

windward upward motion maximum is closer to the coast and has substantially stronger values, while the leeward convergence zone moves further inland with an intensity similar to the case without shear.

Although these conclusions regarding the effect of vertical shear need to be verified observationally, they suggest a possible aid in the prediction of thunderstorms which result from sea breeze convergence. As found by Pielke (1974a), the sea breeze convergence zones are the preferred locations for thunderstorm development and movement on synoptically undisturbed days over south Florida. Assuming the intensity of thunderstorm activity is strongly correlated with sea breeze convergence, as seems likely, the occurrence of thunderstorms with easterly low-level synoptic flow will be enhanced along the Florida east coast when the large-scale winds become more westerly with height, while thunderstorm activity will be diminished along the west coast when the winds become more easterly with height.

#### 4. Comparison with observations

As shown in the last section, the predicted growth of the planetary boundary layer and the subsequent predicted motion fields appear to be physically consistent and qualitatively realistic. The quantitative validity of the solutions using this new planetary boundary layer parameterization, however, must be tested. To do this, observational data are required which have sufficient vertical and temporal resolution to describe the entire planetary boundary layer over the course of a day. Moreover, the data must have been

taken over reasonably homogeneous terrain under steady, undisturbed synoptic conditions, so that the observations best satisfy the physical assumptions of the planetary boundary layer model.

The data collected by Clarke *et al.* (1971) during the 1967 Wangara Experiment around Hay, New South Wales, Australia, provide an excellent observation set which fulfills the assumptions of the parameterization scheme. From their report Day 33 was chosen, since it closely fits the assumptions of the parameterization scheme, and because other researchers have used data from that date to compare with their model results. Deardorff (1974) used Day 33 data to compare against results obtained from his three-dimensional boundary layer model, and used the results to aid in the development of the prognostic formula for  $z_i$ . In that paper, using a planetary boundary layer model which had dynamic equations for all the subgrid-scale fluxes, Deardorff obtained good agreement between his predictions and the observed conditions on Day 33.

Although Deardorff's approach undoubtedly represents the physics more realistically than the method presented in this paper, his model requires about 175 h of CDC 7600 time to perform a 12 h daytime boundary layer calculation.

Wyngaard and Coté (1974), in attempting to reduce boundary-layer calculation times, have recently presented their convective boundary layer model results for Day 33 which are  $10^3$  times faster than Deardorff's calculations, and which agree very favorably with observations. Their model is based on a second-order closure for the turbulent fluctuations, with calculation rates of 1 min of CDC 7600 time per 1 h of simulation time, as opposed to  $875 \text{ min h}^{-1}$  for Deardorff's model. The model presented in this paper uses  $1.3 \text{ min h}^{-1}$  on a CDC 6400 for 31 vertical levels which converts to about  $3 \text{ s h}^{-1}$  on the NCAR CDC 7600 when the explicit finite-difference form of the diffusion equations is used, and to about  $0.5 \text{ s h}^{-1}$  when an implicit form is applied. Thus in simulating the mean structure of the convective planetary boundary layer, the technique discussed in this paper is over  $10^2$  times faster than the method described by Wyngaard and Coté. As a result, although the model presented by Wyngaard and Coté needs to be pursued further, one minute of calculation time per one hour of simulation time corresponds, in a mesoscale model, to only one horizontal grid point. In a 33 by 36 horizontal grid lattice as used in the Pielke (1974a) model, this transforms to 1188 min of calculation time for 1 h of simulation.

Therefore, for the foreseeable future, simpler planetary boundary layer parameterizations are required in mesoscale models in which the representation of the turbulent fluxes is only one aspect of the model. Indeed, Deardorff never intended his model to be used directly in a mesoscale model. Rather, it was his intention, in addition to simulating the physics of turbulence, to

use his more complete model for the development of simpler parameterization schemes, as illustrated by his expression for  $z_i$ .

In this section, then, expression (11) for  $z_i$  will be used along with the profile form of the exchange coefficients as discussed in Section 2, to see how well the observations on Day 33 can be simulated with a much simpler model than that of Deardorff. If a reasonable simulation is realized, then the scheme is an accurate technique by which vertical turbulent fluxes can be represented in a mesoscale model, when the assumptions of the scheme are reasonably well fulfilled.

To test the scheme, the model equations (1)–(4) have been reduced to a one-dimensional form given by

$$\frac{\partial u}{\partial t} = -K_z^{(m)} \frac{\partial u}{\partial z} + f_3(v - v_g) - w \frac{\partial u}{\partial z}, \quad (16)$$

$$\frac{\partial v}{\partial t} = -K_z^{(m)} \frac{\partial v}{\partial z} - f_3(u - u_g) - w \frac{\partial v}{\partial z}, \quad (17)$$

$$\frac{\partial \theta_v}{\partial t} = -K_z^{(\theta)} \frac{\partial \theta_v}{\partial z} - w \frac{\partial \theta_v}{\partial z}, \quad (18)$$

$$\frac{\partial q}{\partial t} = -K_z^{(q)} \frac{\partial q}{\partial z} - w \frac{\partial q}{\partial z}. \quad (19)$$

At this point, several additional improvements to the model alluded to in Section 2 will be discussed. First of all, the virtual potential temperature is used in the potential temperature calculation, where

$$\theta_v = \theta(1 + 0.61q).$$

The effect of virtual potential temperatures is to make the Wangara Day 33 thermodynamic sounding somewhat more unstable than it would be if the dry potential temperature were used.

The next several alterations of the model include a different specification of the surface layer nondimensional wind and temperature profile, and a more consistent evaluation of the surface momentum, heat and moisture fluxes.

The nondimensional wind and temperature profiles were changed from those evaluated by Yamamoto and Shimanuki (1966) to those of Businger (1973) because the interpolation formulas were of a simpler form, and the profiles were based on more recent data, which with the improvement in boundary layer measurement techniques and instrumentation, should be more accurate. In unstable air, the nondimensional wind profile for both techniques are similar but differ most substantially in stable air.

The expressions for the nondimensional wind, potential temperature and specific humidity profiles are given by

$$\phi_m = \begin{cases} (1 - 15\xi)^{-1}, & \xi \leq 0 \\ 1 + 4.7\xi, & \xi > 0 \end{cases} \quad (20)$$

$$\phi_q = \phi_H = \begin{cases} 0.74(1-9\xi)^{-1/2}, & \xi \leq 0 \\ 0.74 + 4.7\xi, & \xi > 0 \end{cases} \quad (21)$$

$$\frac{\partial \phi_m}{\partial \xi} = \begin{cases} 3.75\phi_m^5, & \xi \leq 0 \\ 4.7, & \xi > 0 \end{cases} \quad (22)$$

$$\frac{\partial \phi_H}{\partial \xi} = \begin{cases} 8.22\phi^3, & \xi \leq 0 \\ 4.7, & \xi > 0 \end{cases} \quad (23)$$

where

$$\phi_m = \frac{kz}{u_*} \frac{\partial u}{\partial z} \quad \text{and} \quad \phi_H = \frac{kz}{\theta_*} \frac{\partial \theta_v}{\partial z}$$

The integrated version of the profiles are given by

$$u_* = k(u^2 + v^2)^{1/2} / [\ln(z/z_0) - \psi_1], \quad (24)$$

$$\theta_* = k[\theta_v - \theta_v(z_0)] / 0.74[\ln(z/z_0) - \psi_2], \quad (25)$$

$$q_* = k[q - q(z_0)] / 0.74[\ln(z/z_0) - \psi_2], \quad (26)$$

where

$$\psi_1 = \begin{cases} 2 \ln[(1 + \phi_m^{-1})/2] + \ln[(1 + \phi_m^{-2})/2] \\ -2 \tan^{-1} \phi_m^{-1} + \pi/2, & \xi \leq 0 \\ -4.7 \xi, & \xi > 0 \end{cases} \quad (27)$$

$$\psi_2 = \begin{cases} \ln[(1 + 0.74\phi_H^{-1})/2], & \xi \leq 0 \\ -6.35 \xi, & \xi > 0. \end{cases} \quad (28)$$

The variable  $\xi$  is defined as  $\xi = z/L$ , where

$$L = \bar{\theta} u_*^2 / (kg\theta_*).$$

The expressions for  $\phi_m$ ,  $\phi_H$ ,  $\partial \phi_m / \partial \xi$  and  $\partial \phi_H / \partial \xi$  are used to evaluate the exchange coefficients for momentum, heat and moisture above the surface layer in the planetary boundary layer using the polynomial expression developed by O'Brien (1970) given in (9), where

$$K_z^{(m)}|_h = k u_* h / \phi_m$$

$$K_z^{(q)}|_h = K_z^{(\theta)}|_h = k u_* h / \phi_H.$$

The derivative of  $K_z^{(\eta)}|_h$  with height, required in (9), is

$$\frac{\partial}{\partial z} K_z^{(\eta)}|_h = \frac{K_z^{(\eta)}|_h}{L} \left[ \frac{1}{\xi h} - \frac{1}{\phi^{(\eta)}(\xi h)} \frac{\partial \phi^{(\eta)}(\xi h)}{\partial \xi} \right],$$

where the superscript  $\eta$  refers to the particular exchange coefficient.

The form of the  $K_z^{(\eta)}$  profile discussed above is the same as used in Pielke (1974a, b) and as discussed in Section 2, except for the different formulas for  $\phi_m$ ,  $\phi_n$ ,  $u_*$ ,  $\theta_*$  and the additional calculation of  $q_*$ . The manner in which the  $K_z^{(\eta)}$ 's are used to evaluate the vertical turbulent fluxes is somewhat different, however. If the grid point at which the flux term is evaluated is within the surface layer and is at the lowest level above the ground at which the flux term is evaluated, then the

explicit surface layer flux form given by

$$\left. \begin{aligned} K_z^{(m)} \frac{\partial u}{\partial z} &= u_* |z, & K_z^{(m)} \frac{\partial v}{\partial z} &= u_* |z^2 \\ K_z^{(\theta)} \frac{\partial \theta_v}{\partial z} &= u_* \theta_*, & K_z^{(q)} \frac{\partial q}{\partial z} &= u_* q_* \end{aligned} \right\}$$

is used. If, on the other hand, the grid point is above the lowest level at which the flux term is evaluated, the value of  $K_z^{(\eta)}$  is calculated from (9) and multiplied by the vertical gradient of the appropriate dependent variable as was done in the past. In the special case where the grid point is the lowest one above the ground, but is still above the surface layer, the exchange coefficient is still evaluated using (9), but the vertical gradient term is calculated using surface layer similarity theory as given by

$$\left. \begin{aligned} K_z^{(m)} \frac{\partial u}{\partial z} &= K_z^{(m)} \frac{u_* |z \phi_m}{kz}, & K_z^{(m)} \frac{\partial v}{\partial z} &= K_z^{(m)} \frac{u_* |z \phi_m}{kz} \\ K_z^{(\theta)} \frac{\partial \theta_v}{\partial z} &= K_z^{(\theta)} \frac{\theta_* \phi_H}{kz}, & K_z^{(q)} \frac{\partial q}{\partial z} &= K_z^{(q)} \frac{q_* \phi_H}{kz} \end{aligned} \right\}.$$

This last technique is required because evaluating the vertical derivative between the ground and the next grid level above in the standard finite-difference fashion, assumes that a linear gradient exists between that level and the ground. Using this technique in the model comparisons with the Wangara data resulted in excessive fluxes. Therefore, it was decided to use the surface layer profile functions as a better estimate of the derivative at the first grid point above the ground.

With the aforementioned improvements, the one-dimensional planetary boundary layer model was integrated using the potential temperature and specific humidity profiles, and the geostrophic wind and wind shear as observed at 0900 EST on Day 33 of the Wangara Experiment. The virtual potential temperature and specific humidity at the surface during the day,  $\theta_{vs}$  and  $q_s$ , were obtained from Figs. 1(a) and 2(a) of Deardorff (1974) and from personal communication with Deardorff, where his values were calculated from soil-air heat and moisture budget equations.

Since the surface layer formulas require temperature and specific humidity at  $z_0$  rather than at the surface, expressions for  $\theta_v(z_0)$  and  $q(z_0)$  as a function of  $\theta_{vs}$ ,  $q_s$ ,  $u_*$  and  $\theta_*$ , based on the work of Zilitinkevich (1970), were used. Deardorff (1974) used an equivalent form in his model. In terms of the current model, the formulas for  $\theta_v(z_0)$  and  $q(z_0)$  are

$$\theta_v(z_0) = \theta_{vs} + 0.0962 \frac{\theta_* (u_* z_0)^{0.45}}{k v},$$

$$q(z_0) = q_s + 0.0962 \frac{q_* (u_* z_0)^{0.45}}{k v}.$$

TABLE 1. Predicted values of  $\theta_{vs}$  and  $q_s$  for Day 33 of the Wangara Experiment (from Deardorff).

Time	$\theta_{vs}$ (°C)	$q_s$ (g kg <sup>-1</sup> )
0900	11.5	4.3
1000	21.1	6.1
1100	28.8	5.5
1200	27.5	5.2
1300	28.33	5.05*
1400	27.1	4.9
1500	23.15	4.5*
1600	19.99	4.1
1700	15.70	3.75
1800	9.11	3.75*

Values of  $\theta_{vs}$  and  $q_s$  as a function of time are given in Table 1. The values with asterisks were not available from Deardorff and were therefore estimated from the data he provided. Since  $\theta_*$ ,  $u_*$ ,  $q_*$ ,  $\theta_v(z_0)$  and  $q(z_0)$  are implicit functions of one another, they were solved by an iterative technique analogous to that described by Pielke (1974a).

The geostrophic velocities at the surface ( $u_g=5.34$  m s<sup>-1</sup> and  $v_g=0.43$  m s<sup>-1</sup>), as listed on p. 227 of the Wangara Report, observed at 0900 LST, are assumed constant throughout the integration. The vertical shears of the geostrophic wind, also assumed constant, are given by

$$\frac{\partial u_g}{\partial z} = \begin{cases} 0, & z < \hat{z}_i \\ 2.98 \text{ m s}^{-1} \text{ km}^{-1}, & \hat{z}_1 \leq z < 1 \text{ km} \\ 1.49 \text{ m s}^{-1} \text{ km}^{-1}, & 1 \text{ km} \leq z < 2 \text{ km} \\ 0, & z \geq 2 \text{ km} \end{cases}$$

$$\frac{\partial v_g}{\partial z} = \begin{cases} 0, & z < \hat{z}_i \\ -0.04 \text{ m s}^{-1} \text{ km}^{-1}, & \hat{z}_i \leq z < 1 \text{ km} \\ 0.26 \text{ m s}^{-1} \text{ km}^{-1}, & 1 \text{ km} \leq z < 2 \text{ km} \\ 0, & z \geq 2 \text{ km} \end{cases}$$

TABLE 2. Observed values of  $w$  (cm s<sup>-1</sup>) at various levels for Day 33 of the Wangara Experiment.

Time	$w$ at 500 m	$w$ at 1000 m	$w$ at 1500 m
0900	0.8	0.3	-0.9
1000	-0.3	-1.7	-2.8
1100	0.2	-0.1	-0.1
1200	0.3	0.6	1.1
1300	0.3	1.6	1.5
1400	-0.4	-1.4	-2.5
1500	1.5	1.5	0.5
1600	-1.2	-3.6	-3.7
1700	-1.2	-2.1	-2.4
1800	-0.4	-1.1	-1.4

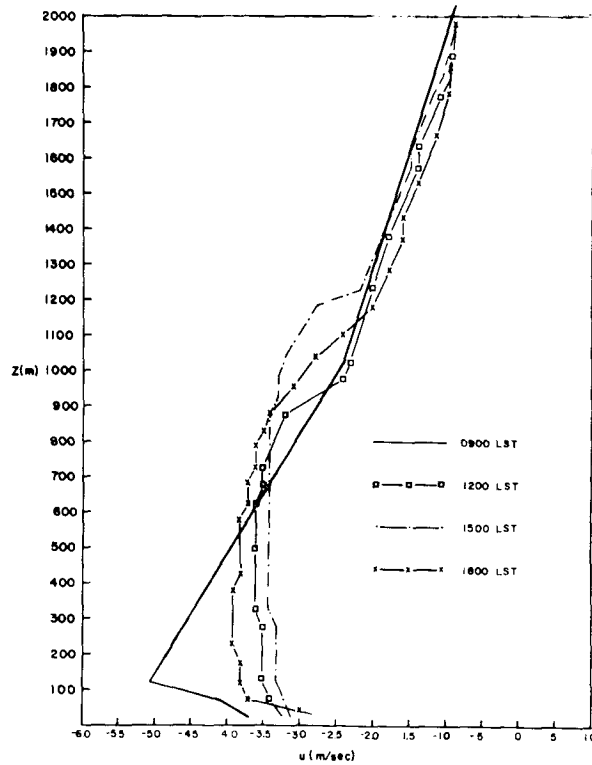


FIG. 15. The predicted east-west velocity profile for Day 33 of the Wangara Experiment (31 levels).

The vertical velocities  $w$  at each level for each hour were obtained from the Wangara Report and linearly interpolated for values between the hour. The values of  $w$  at three selected levels for the ten observation times, are illustrated in Table 2. As evident in the table, up and down motion alternated until after 1500 LST when subsidence became dominant.

The surface roughness  $z_0$  was taken as 1.2 cm, as listed for station 5 on p. 21 of the Wangara Report.

The time evolution of the boundary layer was then predicted using the observed initial thermodynamic vertical structure, the observed geostrophic wind and geostrophic wind shears, the observed vertical velocities, and the surface potential temperatures and specific humidities, as predicted from Deardorff's surface thermal-energy and moisture balance. The model had 31 levels which correspond to the number of levels at which observations were made.

The observed and predicted  $u$  components of the wind are given in Figs. 15 and 16. The predicted east-west velocity shown in Fig. 15 decreases in speed below 600 m after the initial time as the layer becomes well-mixed, while above that level, the winds increase in speed as the boundary layer deepens.

The observed east-west velocity field in Fig. 16 is much more irregular, possibly due to observational errors in the technique used to determine the winds, or as a result of the interpolation technique to obtain

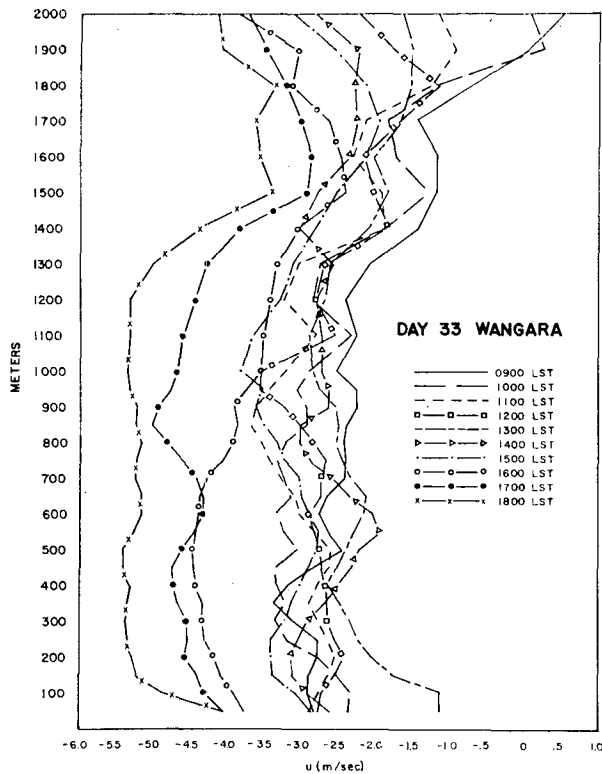


FIG. 16. The observed east-west velocity profile for Day 33 of the Wangara Experiment.

winds at 50 m intervals from balloon positions every 30 s. More likely, however, the irregular wind field is a result of advective effects, turbulent effects, and pressure gradient forces which are not considered in this form of the model. Undoubtedly, even over what appears to be horizontally homogeneous terrain, disturbances propagate in from outside, while irregularities are generated in the motion field by slight horizontal irregularities in the terrain. Evidence of transient disturbances is found in the observed  $w$  field where upward and downward motion alternated during the day, suggestive of waves propagating through the observation network. Use of three-dimensional boundary layer models will be required to describe these events.

After 1300 LST in the lower layer, and after 1500 LST in the upper layer, the observed wind speeds strengthen significantly so that by 1759, the winds below 1200 m are generally greater than  $5 \text{ m s}^{-1}$  from the east. Since the wind speeds increase even above the boundary layer, larger-scale forcing has undoubtedly become important. The  $v$  component of the wind (Figs. 17 and 18) shows only rough agreement between the predictions and observations. The tendency for the winds to become more southerly with time below 1400 m is predicted by the model and observed, although there is considerable irregularity in the observed field.

The model apparently does a rather poor job of predicting the details of the wind profile in the boundary

layer, although some of the general features are reproduced. Deardorff's (1974) calculations, as illustrated in Fig. 9 of his paper, also resulted in only qualitative agreement with the general wind profile. Fortunately, however, the development of the potential temperature and specific humidity profiles in the boundary layer are dominated by the surface fluxes of heat and moisture and the overlying stability, rather than the momentum flux, when the surface layer is sufficiently unstable. Thus, in this situation, the details of the wind profiles are not critically important in predicting the growth of the planetary boundary layer.

The predicted thermodynamic profile agrees more favorably with the observations, as can be noted in Figs. 19–24 where the predicted and observed profiles of virtual potential temperature and specific humidity are plotted. The predicted near-surface virtual potential temperature included in Fig. 19 (plotted at  $z=0$ ), was calculated at 1.5 m using (25) and is intended to correspond to the surface value listed by Clarke *et al.* (1971), which was probably measured from the hand-held radiosonde before it was released. The potential temperature distribution with height, both predicted and observed, shows the elimination of a stable layer, which was present near the surface at 0900 LST, with a deep well-mixed layer up to 950 m in the predictions and about 900 m in the observations by 1200 LST. The predicted warming in the layer is almost identical with

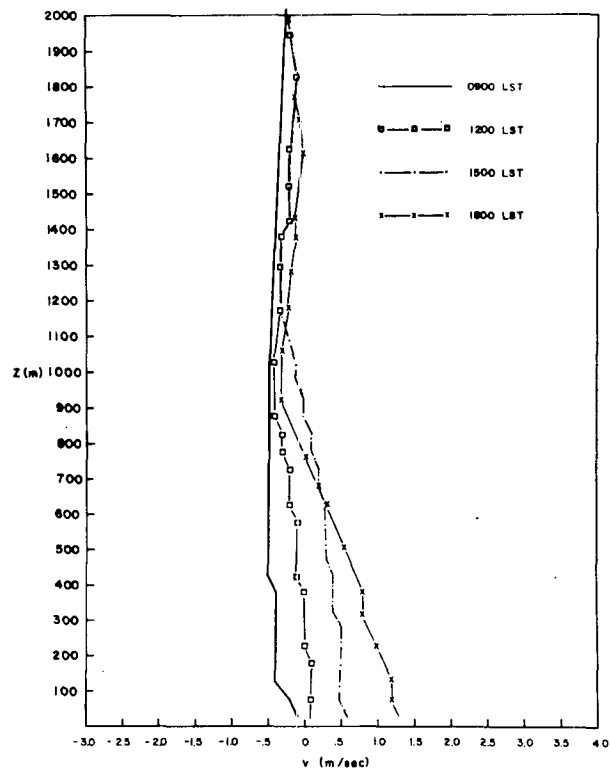


FIG. 17. The predicted north-south velocity profile for Day 33 of the Wangara Experiment (31 levels).

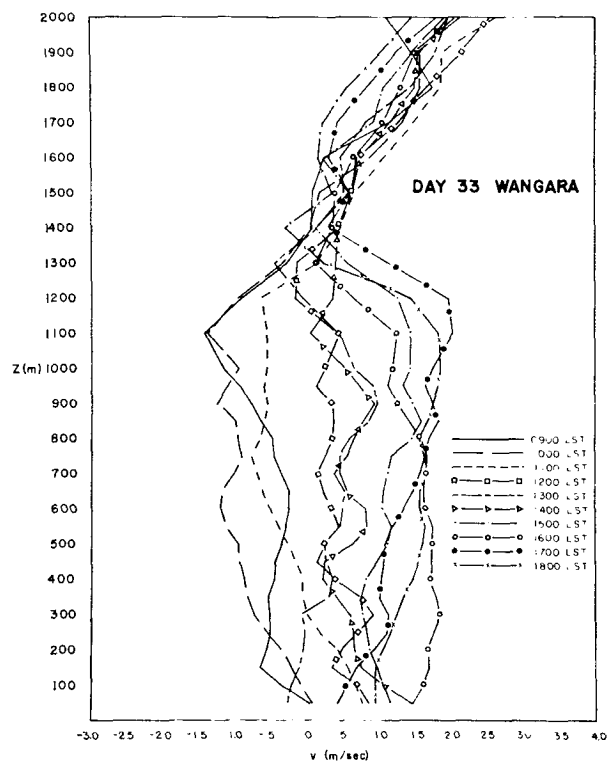


FIG. 18. The observed north-south velocity profile for Day 33 of the Wangara Experiment.

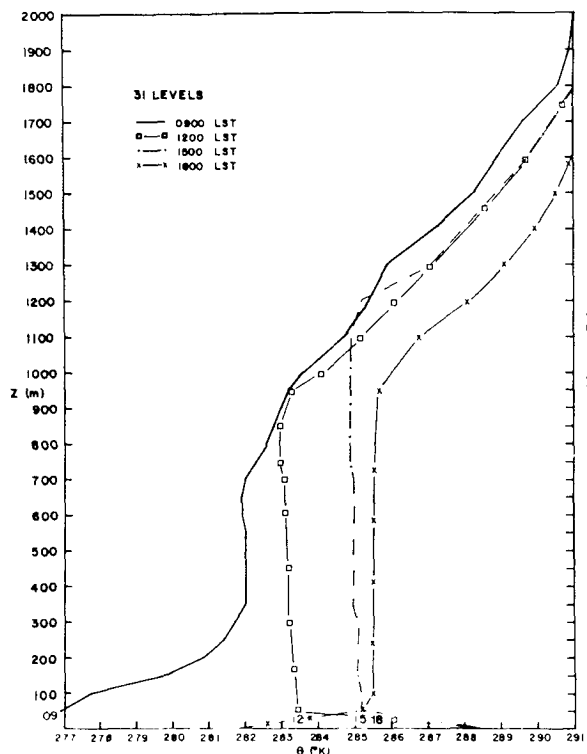


FIG. 19. The predicted potential temperature profile for Day 33 of the Wangara Experiment (31 levels).

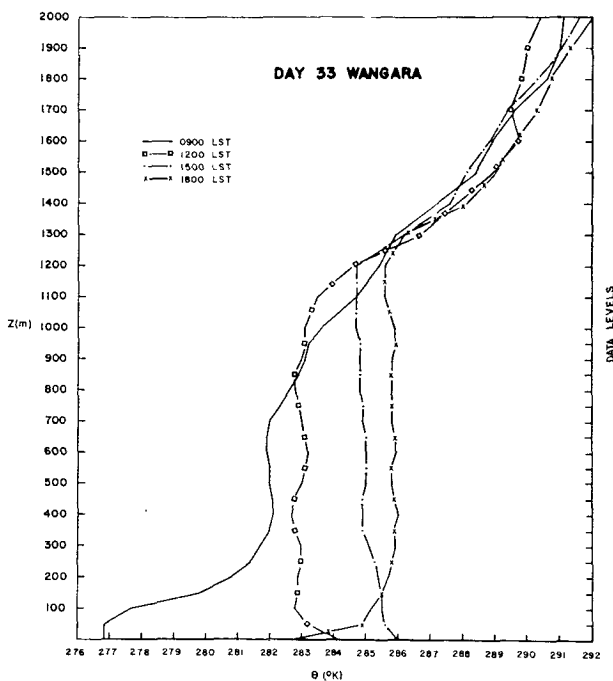


FIG. 20. The observed potential temperature profile for Day 33 of the Wangara Experiment.

the observations. The cooling immediately above the inversion in the observations was not predicted by the model as a result of the prescribed vertical motion included in the calculations, although the observed warming between 1250 and 1700 m was well-simulated.

By 1500 LST, the predicted potential temperature and depth of the mixed layer continued to agree remarkably well with the observations. The potential temperature predicted and observed in the mixed layer was near 285 K. Above the inversion, however, the observed values of potential temperature were nearly the same as the 0900 LST values, whereas the predictions had indicated net warming over most of that layer due to subsidence. The 1800 LST predictions also agreed rather well in the magnitude of the potential temperature in the mixed layer (within about 0.4 K of one another), but substantially underpredicted its depth and overpredicted the warming aloft. Both of these errors are directly attributable to the prescribed vertical motion field obtained from Clarke *et al.* (1971), as seen in Fig. 21, where the model was rerun with the same input as before except the vertical motion was set to zero. Results of this experiment correspond to Deardorff's (1974, Fig. 1a, p. 88) in which large-scale vertical velocities were not included. As illustrated, cooling has occurred relative to the initial sounding, near the top of the mixed layer, in agreement with Deardorff's results, while the strong warming aloft previously predicted could not occur. Since the observations indicate some warming aloft by 1800 LST, but not to the intensity predicted when the observed

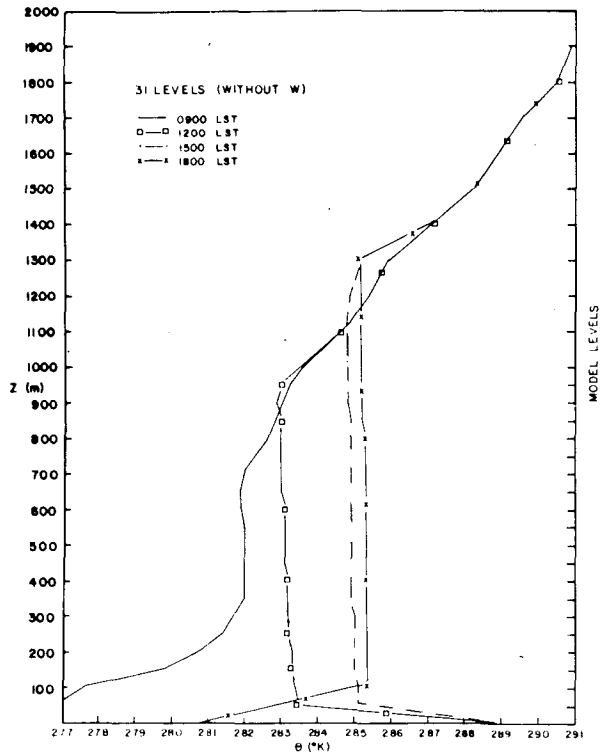


FIG. 21. The predicted potential temperature profile for Day 33 of the Wangara Experiment (31 levels) where  $w$  is set equal zero at all levels.

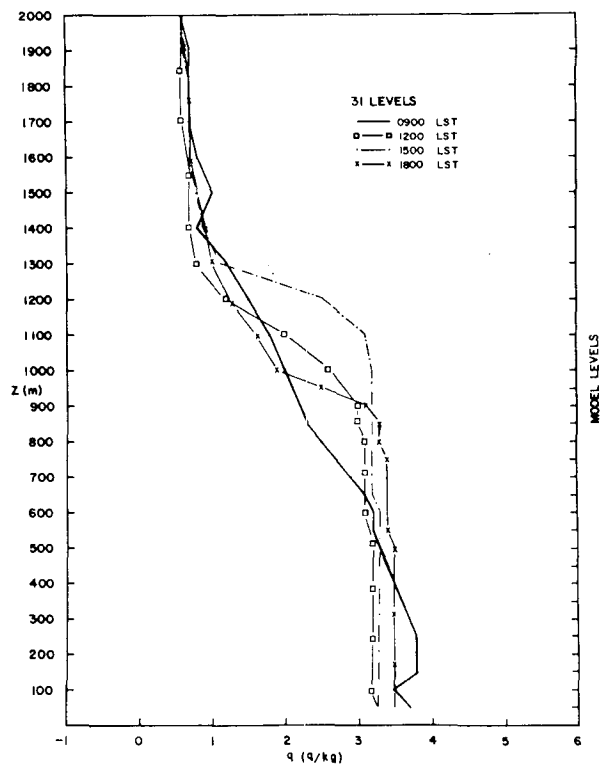


FIG. 22. The predicted specific humidity profile for Day 33 of the Wangara Experiment (31 levels).

vertical velocities are included, one must conclude, assuming the measurements are correct, that cooler potential temperatures were advected into the region after 1500 LST. The thermal wind listed by Clarke *et al.* (1971), however, at 0900 and 2100 (values for the intermediate radiosonde ascent times were not available to Clarke *et al.*) indicates very weak warm advection between the surface and 2 km at the earlier time, and somewhat stronger warm advection later. Unfortunately, as stated by Clarke *et al.* (1971), since three of the stations used to determine the thermal wind are on the coast, the estimates of the large-scale temperature gradient for their observation site, which was far inland, were not highly accurate. Radiational cooling at this level under clear skies would be insufficient to counteract the subsidence warming. Thus, it is impossible to positively determine the reasons for the lack of warming observed in the upper layers, other than speculate that there was cold advection above the boundary layer which was not resolved in the Wangara data. Interestingly, the results at 1800 better agree with the observations above the planetary boundary layer when vertical motion is neglected.

The predicted surface temperature, evaluated at 1.5 m for 1200, 1500 and 1800 LST, tends to be higher or lower than the observed value obtained prior to the radiosonde release, depending on whether the surface layer is unstably or stably stratified. The observed

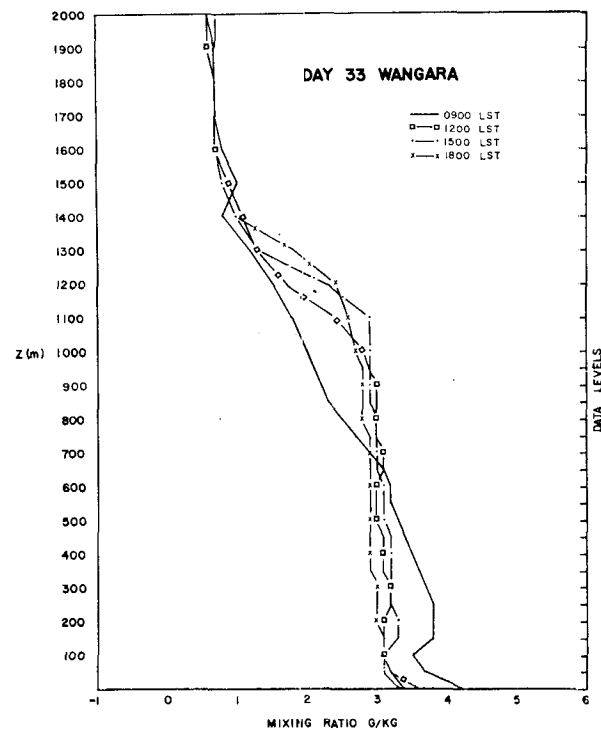


FIG. 23. The observed specific humidity profile for Day 33 of the Wangara Experiment.

temperature would be lower than the predicted if the layer were superadiabatic, and higher if it were subadiabatic, if the actual surface radiosonde reading was made above 1.5 m.

The observed and predicted specific humidity profiles (Figs. 22 and 23) similarly agree favorably, with the best agreement at 1500 LST. At that time, there is drying in the observations below about 675 m and in the predictions below about 500 m, while above those levels the atmosphere becomes more moist. By 1800, however, the agreement again deteriorates due to incorporation of the observed subsidence into the model. As seen in Fig. 24, where the subsidence is excluded from the calculations, the agreement is much better at 1800.

The growth of the planetary boundary layer as predicted by the model presented in this paper with and without  $w$ , by Deardorff's model, and as observed, are given in Fig. 25. The values shown by circled X's are the depths of the well-mixed layer as estimated from the observed potential temperature and specific humidity profiles. The depths plotted from Deardorff's model were estimated from Fig. 6 of his 1974 paper.

As is evident in Fig. 25, the growth of the planetary boundary layer is predicted reasonably well by both Deardorff's more complete model, and by the model discussed in this paper, with and without  $w$ . When  $w$  is

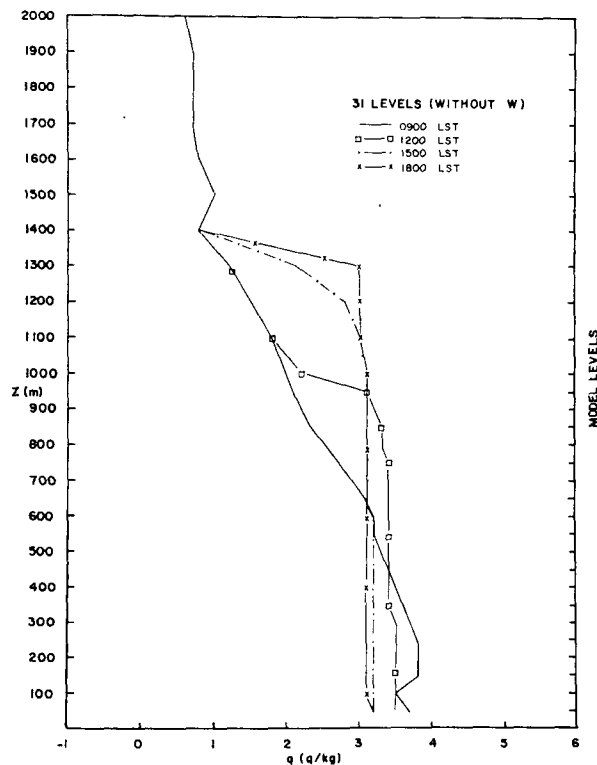


FIG. 24. The predicted specific humidity profile for Day 33 of the Wangara Experiment (31 levels) where  $w$  is set equal to zero at all levels.

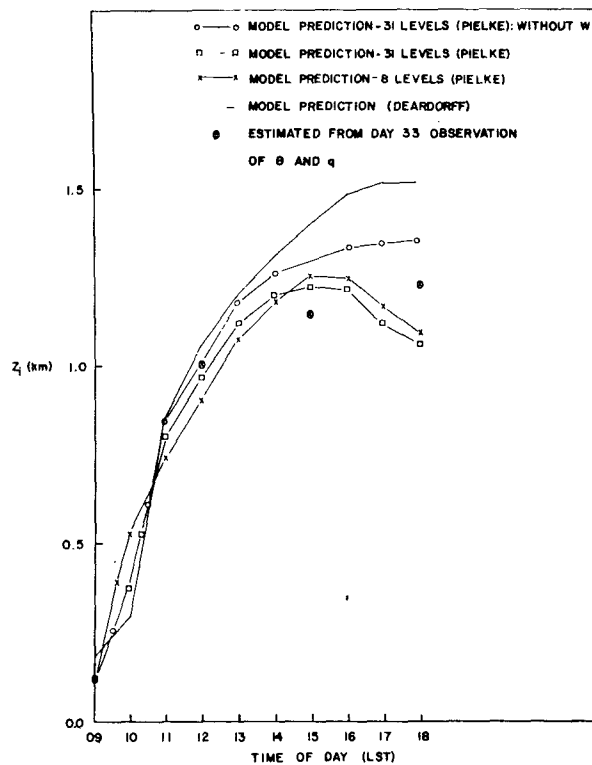


FIG. 25. The observed and predicted depths of the planetary boundary layer on Day 33 of the Wangara Experiment.

included in the calculations, the planetary boundary layer sinks significantly due to the strong subsidence after 1500 so that by 1800 it is less than the observed, whereas without  $w$  it is higher than observed. At 1500 the best prediction of  $z_i$  is made when  $w$  is included. Deardorff (1974) attributed his overprediction of the depth of the planetary boundary layer to the neglect of large-scale subsidence in his calculations. As revealed in the calculations in this paper, however, the incorporation of vertical velocity results in an underprediction of the depth of  $z_i$ , with excessive warming above  $z_i$ . Thus, horizontal advection of temperature, not resolved in the data, likely has negated the effects of vertical motion, particularly after 1500.

Nonetheless, the magnitude of the potential temperature and the specific humidity in the mixed layer is reasonably well-predicted, particularly from 0900 to 1500 LST, with or without the incorporation of  $w$ . The boundary layer depth equation (11) performs a very credible job of simulating the rapid growth of  $z_i$  early in the day as a result of the strong surface heat fluxes with an overlying adiabatic layer from 350 to 700 m. Later in the day, the surface heat flux lessens in intensity and the overlying layer becomes more stable, so the rate of growth of  $z_i$  decreases.

As a result of the experiment presented in this section, it can be concluded that the comparatively simple boundary-layer parameterization scheme de-

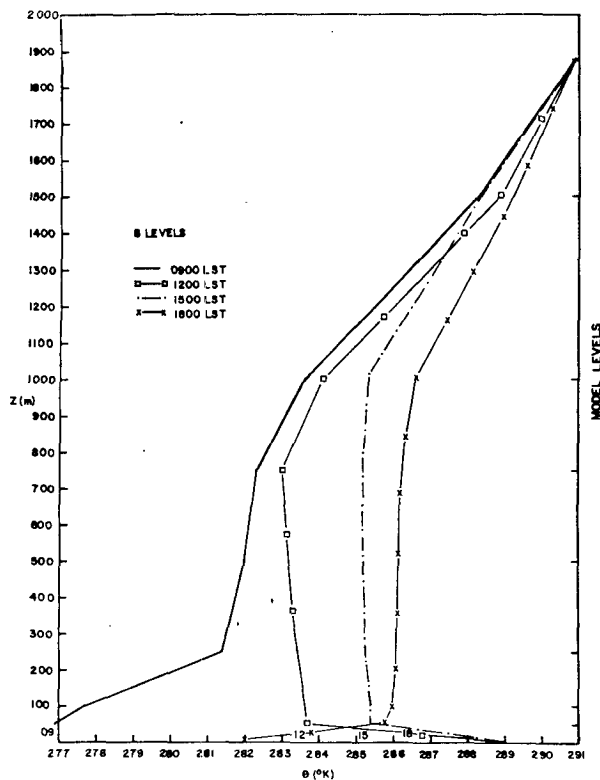


FIG. 26. The predicted potential temperature profile for Day 33 of the Wangara Experiment (8 levels).

scribed in this paper can predict the mean structure of a heated planetary boundary layer, as well as the much more complete and conceptually more sophisticated model of Deardorff (1974)—provided the same number of grid levels are used as there are observation levels. The problems created by the excessive sinking caused by the observed subsidence, however, require that future field measurements of turbulent fluctuations throughout the planetary boundary layer include more elaborate observations in order to monitor thermal advections.

The final experiment in this paper will evaluate the effect of resolution on the boundary layer predictions. The number of levels will be reduced to 8, which is more in line with the maximum resolution reasonably obtainable in most three-dimensional mesoscale prediction models. Selected levels were chosen for this experiment from the observed data, with more resolution below 1000 m than above. The same initial and surface conditions were used as for the 31-level experiment where  $w$  was included. The predicted potential temperature and specific humidity profiles for the 8-level experiment are given in Figs. 26 and 27, while the growth of the planetary boundary layer for the experiment is plotted in Fig. 25. The agreement between the 31-level and the 8-level experiments is rather remarkable with almost identical warming in the boundary layer and very similar changes in the moisture stratification for most

of the integration period. The depth of the planetary boundary layer with 8 levels is almost identical with the 31-level experiment.

The degree of agreement between the 31- and the 8-level experiments is encouraging because it implies that relatively coarse resolution in the boundary layer, using the technique discussed in this paper, can simulate the development of a heated planetary boundary layer remarkably well. This technique will be useful in mesoscale numerical models, and work is under way to incorporate it into the three-dimensional mesoscale model developed by Pielke (1974a).

## 5. Conclusions

This paper uses a prognostic equation suggested by Deardorff (1974) for the growth of the planetary boundary layer to close the parameterization scheme for vertical turbulent mixing in the planetary boundary layer. The following major conclusions were obtained:

- 1) The prognostic equation for the growth of the planetary boundary layer is superior to the diagnostic form used earlier by Pielke (1974a).
- 2) The growth of the planetary boundary layer into a region with substantial vertical shear of the horizontal wind markedly alters the locations of sea breeze convergence zones.
- 3) By improving the boundary layer parameterization scheme given in Pielke (1974a), the simulation of

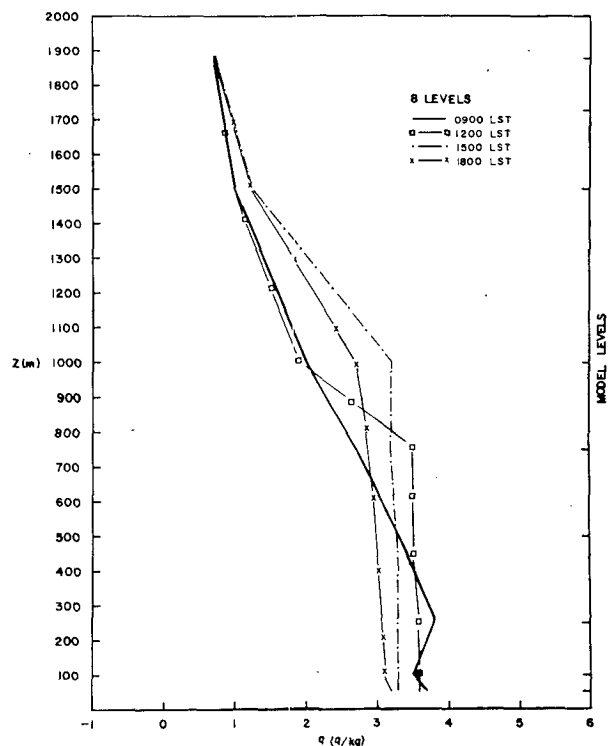


FIG. 27. The predicted specific humidity profile for Day 33 of the Wangara Experiment (8 levels).

vertical turbulent mixing by eddy coefficients which are a function of distance from the ground results in predictions which are as good as those obtained with Deardorff's (1974) much more sophisticated model, and agree favorably with those observed during Day 33 of the Wangara Experiment (Clarke *et al.*, 1971). The inclusion of  $w$ , however, did not improve the results, particularly after 1500 LST, as Deardorff suspected it would, but rather pointed out the lack of resolution of horizontal temperature advections in the Clarke *et al.* (1971) observations.

4) The effect of decreasing the resolution from 31 levels to 8 levels in the boundary layer parameterization scheme does not seriously degrade the solutions, implying the scheme discussed in this paper is a useful tool to represent the heated boundary layer in mesoscale models.

Finally, the use of Deardorff's (1974) equation for the growth of the planetary boundary layer in mesoscale models should result in improved forecasts since the planetary boundary layer is more realistically simulated. His equation will also provide a useful tool in air pollution work, since pollutants are generally confined within the planetary boundary layer.

The representation of the boundary layer presented in this paper has been shown to be useful only during daylight hours, however. During the night, turbulence, under typical conditions, will decay above the surface, and a new planetary boundary layer will develop closer to the ground as a result of longwave radiational cooling. Effort is needed to determine if the profile technique, modified by radiation physics, is applicable to the nocturnal situation.

*Acknowledgments.* The authors extend special thanks to Jim Deardorff for the time he spent answering our specific questions regarding his model and the Wangara observations and for his comments on the final manuscript. Dr. William R. Cotton is also thanked for his review of the manuscript and for making his usual valuable suggestions. The authors also acknowledge the excellent typing by Ms. Bobby Cassidy and Ms. Phyllis Moore, and the professionally performed drafting work of Mr. Bryan Culhane and Mr. Barry Sulkin. The work in this paper was supported under NSF Grant GA-43040X.

## APPENDIX

## List of Symbols

$u$	east-west velocity component	$x$	east-west coordinate
$v$	north-south velocity component	$y$	north-south coordinate
$w$	vertical velocity component	$z$	vertical coordinate
$w_i$	vertical velocity component at the level of the planetary boundary layer	$\theta$	potential temperature
$t$	time	$\theta_v$	virtual potential temperature [ $=\theta(1+0.61q)$ ]
		$\pi$	[ $=C_p(P/P_{00})^\kappa$ ]
		$C_p$	specific heat of air at constant pressure
		$\kappa$	[ $=R/C_p$ ]
		$R$	gas constant of dry air
		$P_{00}$	reference pressure
		$P$	pressure
		$f_3$	Coriolis parameter [ $=2\Omega \sin\phi$ ]
		$f_2$	[ $=2\Omega \cos\phi$ ]
		$\Omega$	angular velocity of the earth
		$\phi$	latitude
		$K_z^{(m)}$	vertical exchange coefficient for momentum
		$K_z^{(h)}$	vertical exchange coefficient for heat
		$K_z^{(q)}$	vertical exchange coefficient for specific humidity
		$K_H$	horizontal exchange coefficient
		$g$	gravitational acceleration
		$q$	specific humidity
		$s$	material surface top of the model
		$w_T$	vertical velocity at top Eulerian level of the model
		$z_T$	top Eulerian level of the model
		$\Delta x$	horizontal grid interval
		$\alpha_{2D}$	adjustment coefficient in the horizontal exchange coefficient
		$z_i$	depth of the planetary boundary layer
		$h$	depth of the surface layer
		$u_*$	surface friction velocity
		$\theta_*$	surface friction temperature (in Section 4, $\theta_*$ is evaluated in terms of virtual potential temperature)
		$\theta_{vs}$	surface virtual potential temperature
		$\partial\theta^+/\partial z$	potential temperature gradient immediately above the planetary boundary layer
		$u_g$	east-west geostrophic velocity
		$v_g$	north-south geostrophic velocity
		( $\hat{\quad}$ )	(i.e. $\hat{\theta}$ , $\hat{z}_i$ , $\hat{\pi}$ , etc.) indicates an initial value of that variable
		$\tau$	corresponds to a given time step
		$\phi_m$	nondimensional wind profile
		$\phi_H$	nondimensional temperature profile
		$\xi$	nondimensional stability height [ $=kgz\theta_*/\bar{\theta}u_*^2$ ]
		$k$	von Kármán's constant ( $k=0.35$ in this paper)
		$q_*$	surface friction specific humidity
		$u_* _x$	east-west component of $u_*$ [ $=u_* \cos\psi$ ]
		$u_* _y$	north-south component of $u_*$ [ $=u_* \sin\psi$ ]
		$w_*$	convective velocity (defined in text)
		$\psi$	$\tan^{-1}(v_1/u_1)$ where $v_1$ and $u_1$ are evaluated at the lowest grid level above the surface
		$q_s$	specific humidity at the surface
		$\nu$	kinematic viscosity of air ( $\nu=0.15 \text{ cm}^2 \text{ s}^{-1}$ )
		$z_0$	surface roughness

## REFERENCES

- Blackadar, A. K., and H. Tennekes, 1968: Asymptotic similarity in neutral barotropic planetary boundary layers. *J. Atmos. Sci.*, **25**, 1015-1020.
- Businger, J. A., 1973: Turbulent transfer in the atmospheric surface layer. *Workshop in Micrometeorology*, Amer. Meteor. Soc., Chap. 2.
- Clarke, R. H., A. J. Dyer, R. R. Brook, D. G. Reid and A. J. Troup, 1971: *The Wangara Experiment: Boundary Layer Data*. Commonwealth Scientific and Industrial Research Organization, Australia, 316 pp.
- Deardorff, J., 1967: Empirical dependence of the eddy coefficients for heat upon stability above the lowest 50m. *J. Appl. Meteor.*, **6**, 631-643.
- , 1973: Three-dimensional numerical modeling of the planetary boundary layer. *Workshop in Micrometeorology*, Amer. Meteor. Soc., Chap. 7.
- , 1974: Three-dimensional numerical study of the height and mean structure of a heated planetary boundary layer. *Boundary Layer Meteor.*, **7**, 81-106.
- , 1975: The development of boundary layer turbulence models for use in studying the severe storm environment. *Open Sesame, Proc. Opening Meeting*, Boulder, Colo., 4-6 September, 1974. D. K. Lilly, Ed., pp. 251-264. [Available from NOAA, ERL, Boulder, Colo. 80302].
- Donaldson, C. du P., 1973: Construction of a dynamic model of the production of atmospheric turbulence and the dispersal of atmospheric pollutants. *Workshop in Micrometeorology*, Amer. Meteor. Soc., Chap. 8, Section VIII.
- Emmitt, G. D., 1975: Momentum redistributions by enhanced mixing over heated islands, Ph.D. dissertation, University of Virginia, 193 pp.
- Estoque, M. A., 1961: A theoretical investigation of the sea breeze. *Quart. J. Roy. Meteor. Soc.*, **87**, 136-146.
- , 1962: The sea breeze as a function of the prevailing synoptic situation. *J. Atmos. Sci.*, **19**, 244-250.
- Lavoie, R. L., 1972: A mesoscale numerical model of lake-effect storms. *J. Atmos. Sci.*, **29**, 1025-1040.
- Lee, J. D., 1973: Numerical simulation of the planetary boundary layer over Barbados, W.I. Ph.D. dissertation, Florida State University, 102 pp.
- Lumley, J. L., and B. Khajeh-Nouri, 1974: *Advances in Geophysics*, Vol. 18A. Academic Press, 169-192.
- McPherson, R. P., 1970: A numerical study of the effect of a coastal irregularity on the sea breeze. *J. Appl. Meteor.*, **9**, 767-777.
- Mellor, George L., and Tetsuji Yamada, 1974: A hierarchy of turbulence closure models for planetary boundary layers. *J. Atmos. Sci.*, **31**, 1791-1806.
- O'Brien, J. J., 1970: A note on the vertical structure of the eddy exchange coefficient in the planetary boundary layer. *J. Atmos. Sci.*, **27**, 1213-1215.
- Orlanski, I., B. B. Ross and L. J. Polinsky, 1974: Diurnal variation of the planetary boundary layer in a mesoscale model. *J. Atmos. Sci.*, **31**, 965-989.
- Pielke, R. A., 1974a: A three-dimensional numerical model of the sea breezes. *Mon. Wea. Rev.*, **102**, 115-139.
- , 1974b: A comparison of three-dimensional and two-dimensional numerical predictions of sea breezes. *J. Atmos. Sci.*, **31**, 1577-1585.
- Shimanuki, A., 1969: Formulation of vertical distributions of wind velocity and eddy diffusivity near the ground. *J. Meteor. Soc. Japan*, Ser. 2, **47**, 292-297.
- Wyngaard, J. C., and O. R. Coté, 1974: The evolution of the convective planetary boundary layer—a higher-order-closure model study. *Bound.-Layer Meteor.*, **7**, 289-308.
- Yamamoto, G., and A. Shimanuki, 1966: Turbulent transfer in diabatic conditions. *J. Meteor. Soc. Japan*, Ser. 2, **44**, 301-307.
- Zilitinkevich, S. S., 1970: *Dynamics of the Atmospheric Boundary Layer*. Leningrad, Gidrometeor., 291 pp.